Combustion Theory and Modelling
Publication details, including instructions for authors and subscription information:
http://www.tandfonline.com/loi/tctm20

PDF calculations of piloted premixed jet flames

David H. Rowinski [a] & Stephen B. Pope [a]
[a] Cornell University, Mechanical and Aerospace Engineering, Ithaca, NY, 14853, USA

Available online: 07 Dec 2010

To cite this article: David H. Rowinski & Stephen B. Pope (2011): PDF calculations of piloted premixed jet flames, Combustion Theory and Modelling, 15:2, 245-266

To link to this article: http://dx.doi.org/10.1080/13647830.2010.535568

Combustion Theory and Modelling
Vol. 15, No. 2, 2011, 245–266

PDF calculations of piloted premixed jet flames

David H. Rowinski* and Stephen B. Pope

Cornell University, Mechanical and Aerospace Engineering, Ithaca, NY 14853, USA

(*Received 19 May 2010; final version received 20 October 2010*)

A series of piloted premixed jet flames with strong finite-rate chemistry effects is studied using the joint velocity-turbulence frequency-composition PDF method. The numerical accuracy of the calculations is demonstrated, and the calculations are compared to experimental data. It is found that all calculations show good agreement with the measurements of mean and rms mixture fraction fields, while the reaction progress is overpredicted to varying degrees depending on the jet velocity. In the calculations of the flame with the lowest jet velocity, the species and temperature show reasonable agreement with the measurements, with the exception of a small region near the centerline where products and temperature are overpredicted and fuel and oxidizer are underpredicted. In the calculations of the flame with the highest jet velocity, however, the overprediction of products and temperature and underprediction of fuel and oxidizer is far more severe. An extensive set of sensitivity studies on inlet boundary conditions, turbulence model constants, mixing models and constants, radiation treatment, and chemical mechanisms is conducted to show that any parameter variation offers little improvement from the base case. To shed light on these discrepancies, diagnostic calculations are performed in which the chemical reactions are artificially slowed. These diagnostic calculations serve to validate the experimental data and to quantify the amount by which the base case calculations overpredict reaction progress. Improved calculations of this flame are achieved only through artificially slowing down the chemical reaction by a factor of about 10. The mixing model behavior in this combustion regime is identified as a likely cause for the observed discrepancy in reaction progress.

Keywords: PDF method; turbulent flames; lean premixed combustion; finite-rate chemical kinetics; detailed chemistry

1. Introduction

The ability of the PDF method [1] to treat chemical reactions exactly has rendered it a useful tool for the prediction of finite-rate chemistry effects in turbulent flames. Past studies have shown the PDF method to be capable of calculating non-premixed jet flames [2,3], including flames exhibiting combustion phenomena such as local extinction and reignition [4–8]. Similarly, the PDF method has successfully been applied to stoichiometric premixed planar flames [9] and jet flames [10]. In the current work, the PDF method is applied to a series of piloted premixed jet flames [11–13] which exhibit high turbulence levels, wide reaction zones, and extinction-reignition events, while based on a burner of simple geometry using a lean premixed fuel jet. While there exist other approaches specifically for modeling

*Corresponding author. Email: dhr46@cornell.edu

ISSN: 1364-7830 print / 1741-3559 online

DOI: 10.1080/13647830.2010.535568
http://www.informaworld.com

Table 1. Properties of the three concentric streams in the PPJB: D is diameter, U_b is jet bulk velocity, T is temperature, ϕ is equivalence ratio. The two flames considered, PM1-50 and PM1-200, have jet velocities of 50 m/s and 200 m/s, respectively.

Stream	D (mm)	U_b (m/s)	T (K)	ϕ	Composition
Jet	4	50–200	300	0.5	CH_4–air (unburnt)
Pilot	23.5	5.3	2280	1	CH_4–air (burnt)
Coflow	197	4.0	1500	0.43	H_2–air (burnt)

premixed flames, the PDF approach is not inherently limited to a particular mode of combustion.

Lean premixed combustion is of practical interest as a means of pollutant reduction. A prominent feature of lean premixed combustion is the low temperature at which combustion occurs. Consequently, there is decreased formation of pollutants such as NO_x, soot, and volatile organic compounds. However, operation at lean equivalence ratios also has the complication of increased tendency for extinction or blowoff, and the details of the combustion can be extremely sensitive to fuel composition [14]. For these reasons, a better understanding of the turbulence-chemistry interaction in this regime is critical.

The flames studied here are based on the Sydney piloted premixed jet burner (PPJB) [11]. The burner consists of a central jet of a lean methane–air premixture surrounded by a pilot of hot stoichiometric methane–air products. Outside the pilot stream is a hot coflow of lean hydrogen–air products. The stream configurations in the PPJB are summarized in Table 1. There is an additional coflow of ambient air around the hot coflow stream. However, additional calculations of the four-stream problem (shown in the supplemental material in Figure SM-1, where Figure SM-1 denotes Figure 1 of the supplemental material) reveal that the entire flame lies well within the hot coflow of lean hydrogen products, and there is little difference when the additional air stream is not considered. Therefore, the air stream is neglected in these calculations. The problem is then reduced to a three-stream problem. A mixture fraction is associated with each stream, and is defined to be a passive scalar that is unity at the composition of that stream, and zero at the composition of the other streams. The mixture fractions sum to unity, so there are only two independent mixture fractions. In practice, the mixture fractions are defined based on the elemental specific moles of H, O, and C.

Four flames are measured in [11], and the flames with the lowest and highest jet velocities, PM1-50 and PM1-200, are presented here. PM1-50 has a central jet with bulk velocity of 50 m/s and Reynolds number (Re) of 12,500 based on the central jet. The configuration of PM1-200 is identical to that of PM1-50, except that the central jet bulk velocity is 200 m/s, yielding a Reynolds number of 50,000. PM1-200 exhibits a decreased luminosity downstream from x/D of 15–45, where x is the axial coordinate and $D = 4$ mm is the central jet diameter. This region is referred to here as an extinction region. Farther downstream, between x/D of 45 and 60, there is a small increase in luminosity, referred to here as a reignition region.

This work is outlined as follows: First, in Section 2, a brief description of the models and numerical methods used in the calculation is presented. In Section 3, the numerical and model parameters used in the calculations are stated, and the level of numerical accuracy is reported. In Section 4, results are presented for the base case, and the findings of a large number of sensitivity studies are summarized. The sensitivity of the flames to the chemical reaction timescale is shown, and the results are discussed in detail. Conclusions are drawn

in Section 5 regarding the performance of the models and the nature of the combustion in these flames. Additionally, the supplemental material contains many more results than can be presented in this paper.

2. PDF method

In the joint velocity-turbulence frequency-composition PDF method [15], the joint PDF of fluctuating velocity, turbulence frequency, and composition is solved by a particle-based Monte Carlo method. Particle velocities are modeled by the simplified Langevin model [16], and the timescale of turbulence is provided by a stochastic frequency model [17].

The particle composition evolves by mixing and reaction. In the base case, the EMST (Euclidean Minimum Spanning Tree) mixing model [18] is used to advance the particle composition due to mixing. A chemical mechanism dictates the reaction rates through which the particle composition advances due to chemical reaction; this step is performed in a computationally efficient way by using the ISAT (*In Situ* Adaptive Tabulation) algorithm [19,20] to build a storage-retrieval table as the calculation progresses. The parallel algorithm of domain partitioning of particles [7] is used to facilitate efficient parallel computation.

The particle solver is coupled with a finite volume solver which solves the mean equations of mass, momentum, energy, and state [21–23]. The finite volume solver provides the particle solver with the mean velocity and pressure, while the particle solver provides the turbulence quantities and reaction source term to the finite volume solver. These models and solvers are the same used in many previous calculations [7, 8, 23] with the same model constants, excluding the turbulence model parameter $C_{\omega 1}$, as discussed later.

3. Calculation details

3.1. *Computational domain and boundary conditions*

The solution domain is a rectangle represented in polar cylindrical coordinates. The origin corresponds to the center of the central jet at the jet exit plane. The domain extends $40D$ in the radial (r) direction and $100D$ in the axial (x) direction. The coflow boundary ($r/D = 40$) is taken to be a perfect-slip wall, the centerline ($r/D = 0$) is axisymmetric, and at the outflow ($x/D = 100$) the mean pressure is uniform.

At the inflow plane ($x/D = 0$), the mean velocities are prescribed based on separate calculations using the commercial code FLUENT. The $k - \varepsilon$ model is used on a domain similar to that used for the joint-PDF calculations, but extending $100D$ upstream of the jet exit plane. The velocity profiles at the jet exit plane are extracted to represent the fully developed pipe flow of the jet and the entrainment of the pilot and coflow. The variances of velocity, $\langle u_x u_x \rangle$, $\langle u_r u_r \rangle$, and $\langle u_\theta u_\theta \rangle$, are approximated based on the turbulent kinetic energy, k, according to $\langle u_x u_x \rangle = k$ and $\langle u_r u_r \rangle = \langle u_\theta u_\theta \rangle = (1/2)k$. The velocity covariance, $\langle u_x u_r \rangle$, is prescribed based on the turbulent viscosity, ν_T, and the gradient of the mean axial velocity in the radial direction, $\partial \langle U_x \rangle / \partial r$, according to $\langle u_x u_r \rangle = -\nu_T \partial \langle U_x \rangle / \partial r$. The mean velocity profiles, the axial variance of velocity, and the velocity covariance are shown in Figure 1 for the base case calculations of PM1-200.

The compositions are prescribed based on the experimental conditions given in Table 1, and the coflow and pilot are taken to be in chemical equilibrium. For the base case, the mean temperature profiles at the inlet are uniform for each stream. Additionally, the heat transfer between the hot coflow and the cold, pre-ignited pilot stream through the coflow-pilot wall

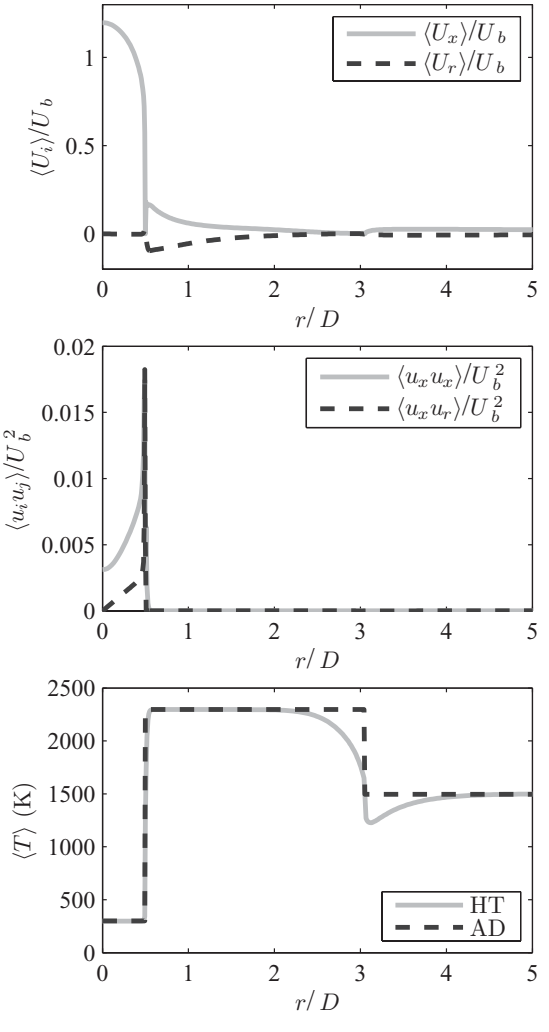

Figure 1. Inlet profiles from FLUENT calculations for flame PM1-200. The topmost plot shows the profiles at the inlet plane for mean axial velocity, $\langle U_x \rangle$, indicated by the solid line, and mean radial velocity, $\langle U_r \rangle$, indicated by the dashed line. Quantities are non-dimensionalized by the jet bulk velocity, U_b, and the jet diameter, D. The middle plot shows the inlet profiles of the axial variance of velocity, $\langle u_x u_x \rangle$, indicated by the solid line, and the covariance, $\langle u_x u_r \rangle$, indicated by the dashed line. The bottom plot shows the mean temperature profiles for the case considering heat transfer, indicated by the solid line, and for the adiabatic base case, indicated by the dashed line.

is considered in subsequent calculations. The temperature profiles for these two cases are compared in Figure 1 for the calculations of PM1-200.

It is emphasized that the FLUENT calculations are used solely to obtain these inflow boundary conditions for the PDF calculations. Furthermore, although some of the turbulence quantities are crudely approximated, it is found from sensitivity studies that the inlet conditions make little difference in the region of interest in these calculations, generally beyond 25 jet diameters downstream.

Table 2. Results of numerical convergence tests. Shown are the maximum percentage changes (relative to the base case) in the mean and rms of various quantities for tests A, B, C, and D. In case A, the grid is refined from (N_x,N_r) of (144,144) to (192,192); in case B, N_{pc} is increased from 50 to 200; in case C, ϵ_{tol} is reduced from 2×10^{-5} to 1×10^{-5}; in case D, N_{ta} increases from 4000 to 8000.

	ξ		T		Y_{maj}		Y_{min}	
Case	ϵ_{mean}	ϵ_{rms}	ϵ_{mean}	ϵ_{rms}	ϵ_{mean}	ϵ_{rms}	ϵ_{mean}	ϵ_{rms}
A	4%	8%	4%	7%	7%	10%	8%	15%
B	1%	3%	1%	2%	1%	3%	2%	7%
C	1%	1%	1%	1%	1%	2%	1%	3%
D	1%	2%	1%	2%	1%	1%	2%	3%

3.2. *Base case*

3.2.1. *Numerical parameters*

Numerical error is present in the calculations due to the finite number of cells in the axial and radial directions, N_x and N_r, particles per cell, N_{pc}, iterations of time averaging, N_{ta}, and due to the ISAT error tolerance, ϵ_{tol}, being greater than zero. In the base case, these parameters are taken to be: $N_x = N_r = 144$, $N_{pc} = 50$, $N_{ta} = 4000$, and $\epsilon_{tol} = 2 \times 10^{-5}$. The error in the calculations is examined through convergence studies of these four parameters in PM1-200. The reported error between two cases is defined as the maximum percentage difference relative to the peak value, at all investigated locations. The results of the convergence studies are summarized in Table 2, showing the maximum errors in mixture fractions ξ, temperature T, and mass fractions of major (CH_4,O_2,N_2,CO_2,H_2O) and minor (CO, OH) species, Y_{maj} and Y_{min}. In case A, the grid is refined from (N_x,N_r) of (144,144) to (192,192); in case B, N_{pc} is increased from 50 to 200; in case C, ϵ_{tol} is reduced from 2×10^{-5} to 1×10^{-5}; in case D, N_{ta} increases from 4000 to 8000. As may be seen, the only significant numerical error is due to the grid size (case A). This error is generally of order 5% for mean quantities and 10% for rms quantities, although slightly higher for minor species.

3.2.2. *Model parameters*

The value for the turbulence model parameter $C_{\omega 1}$, which controls the spreading rate of the jet, is determined from calculations of non-reacting flows on the same burner configuration. The value $C_{\omega 1} = 0.70$ is chosen, and the agreement of velocity in the non-reacting flows is good. This value of $C_{\omega 1}$ is larger than the values of 0.65 used in [7, 8] and 0.56 in [5]. The EMST mixing model with a mixing constant, C_ϕ, of 1.5 is used for the base case, along with the ARM1 16-species reduced mechanism for methane [25]. This mixing model, value of C_ϕ, and mechanism have previously yielded successful calculations of non-premixed jet flames [7].

4. Results and discussion

4.1. *Base case*

A brief summary of the base case for both flames is provided first. Figure 2 shows profiles of scalar statistics for the base case calculations of PM1-50 at the two farthest downstream measurement locations, $x/D = 15$ and $x/D = 25$. The base case for PM1-50 is generally marked by good agreement in the mean and rms of all mixture fractions, fuel, oxidant,

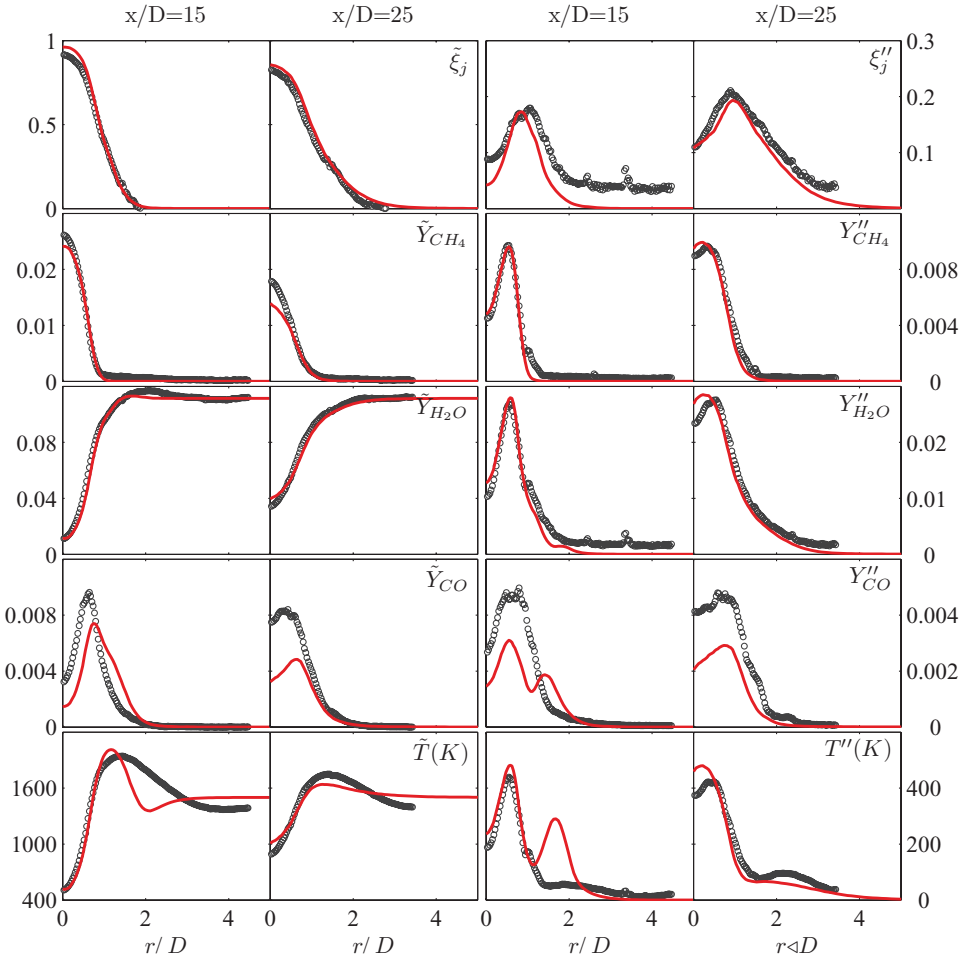

Figure 2. Radial profiles of Favre mean and rms mass fractions (Y) and temperature (T) for the base case of PM1-50 at $x/D = 15$ and $x/D = 25$. Open circles are measurements, solid lines are the base case calculations. To see the full colour versions of this and subsequent figures, please access the online version of this paper.

and products. Near the centerline at $x/D = 25$, there is a small region where the reaction progress is overpredicted. One shortcoming is an inaccurate calculation of the initial mixing between the pilot and coflow. This can be observed both in the faster spreading of the temperature profile in the calculations and also in the larger variances produced between the pilot and the coflow in the calculations. These discrepancies are observed at $x/D = 15$ and further upstream. However, sensitivity studies show that the inlet conditions make little difference beyond $x/D = 25$ in PM1-50, and far less difference in PM1-200. Scatter plots of the radicals CO and OH (shown in the supplemental material, Figure SM-5) as a function of equivalence ratio, ϕ, suggest that most reaction occurs around ϕ of 0.6–0.7. This range of equivalence ratios is slightly richer than than central jet, where ϕ is 0.5, suggesting that in general the combustion occurring in this flame is sustained by richer mixtures.

The base case for PM1-200 is markedly different. Figure 3 shows the scalar statistics in the base case calculations of PM1-200 at the two farthest downstream measurement

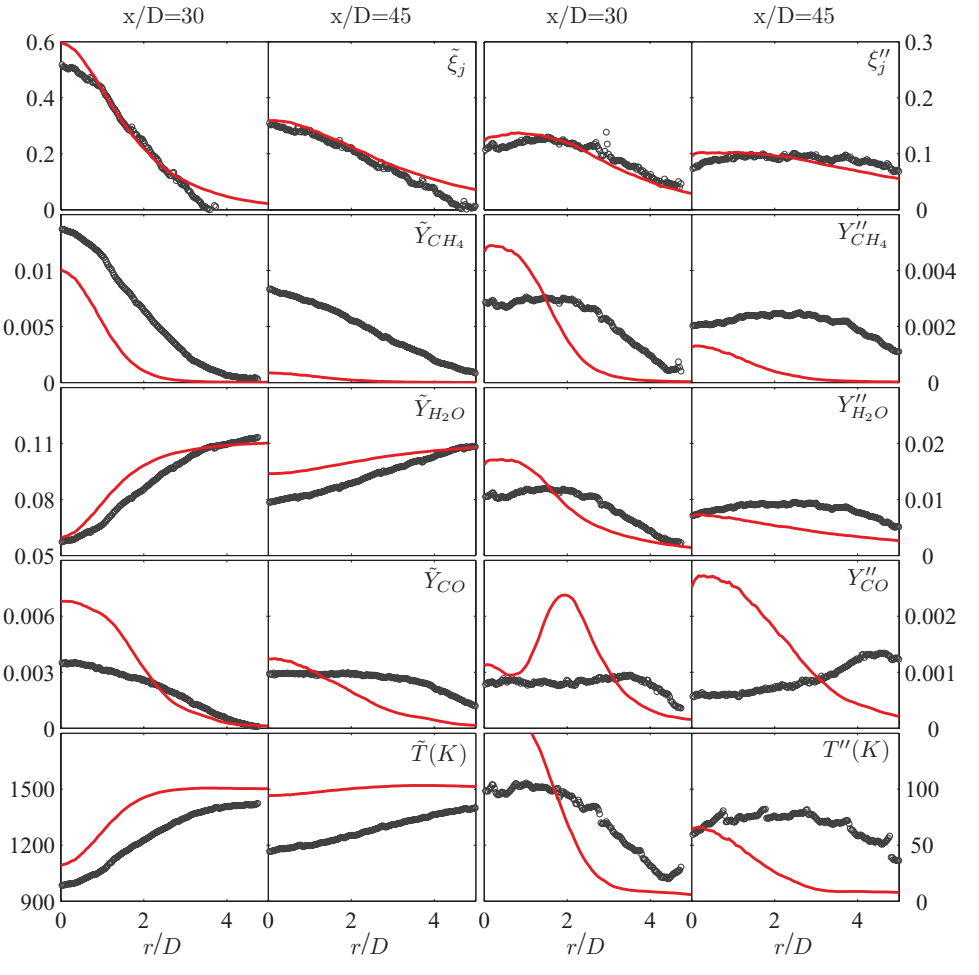

Figure 3. Radial profiles of Favre mean and rms mass fractions (Y) and temperature (T) for the base case of PM1-200 at $x/D = 30$ and $x/D = 45$. Open circles are measurements, solid lines are the base case calculations.

locations, $x/D = 30$ and $x/D = 45$. While all mean and rms mixture fractions show good agreement, the fuel and oxidant are drastically underpredicted while the products and temperature are overpredicted downstream. These calculations involve three streams, namely the jet, pilot, and coflow. A mixture fraction is associated with each stream and is evaluated in the calculations. It is important to note that the mean and rms of all three mixture fractions is generally well-predicted, so that the observed differences are not caused by inaccurate calculations of the mixing but rather by the overprediction of the progress of the reaction. To examine the influence of model parameters on this discrepancy, sensitivity studies are conducted.

4.2. *Sensitivity studies*

An extensive set of sensitivity studies is performed on PM1-200. The details of these studies are provided in the supplemental material in Figures SM-24–62. These studies

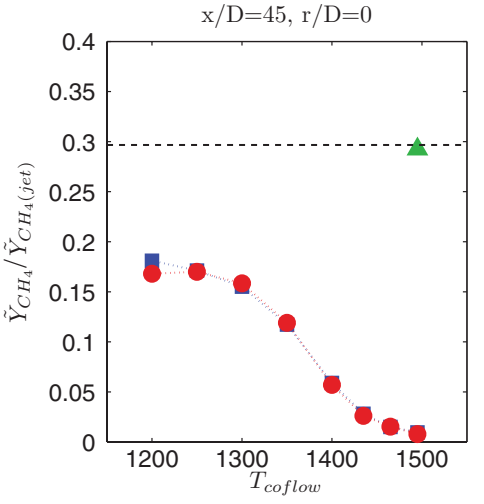

Figure 4. Mean fuel mass fraction normalized by the fuel mass fraction of the jet, at $x/D = 45$ on the centerline as a function of coflow temperature in calculations of PM1-200. Squares indicate the ARM-1 mechanism, and circles indicate the UCSD mechanism. The triangle corresponds to the inert case. The experimental measurement is shown as the dashed line.

are summarized here. Several inlet velocity profiles are compared (Figures SM-24–26), including velocity profiles generated from FLUENT calculations of varying geometric detail, and profiles of simple plug flows and fully developed pipe flows. A wide range of pilot temperatures (2230–2330 K) is examined (Figures SM-27–29). The heat loss from the coflow to the unreacted pilot stream is investigated by modeling the heat transfer in the FLUENT calculations for the inlet profiles. Overall, the effect of all these inflow conditions on the level of reaction downstream is small.

The model parameters are also investigated in the sensitivity studies. The value of $C_{\omega 1}$ is varied between 0.65 and 0.75 (Figures SM-33–35). A wide range of values of C_ϕ (1–12) is investigated with the base case EMST mixing model (Figures SM-36–41), in addition to the modified Curl (MC) [26,27] and interaction-by-exchange-with-the-mean (IEM) [28,29] mixing models (Figures SM-42–53). The influence of the chemical mechanism is studied (Figures SM-54–59) with mechanisms ranging from a five-step reduced mechanism [25] to the detailed GRI3.0 mechanism [30].

A wide range of coflow temperatures from 1200 K to 1500 K is investigated with two different chemical mechanisms, namely ARM-1 from the base case, and the UCSD mechanism [31]. Shown in Figure 4 is the mean fuel mass fraction at $x/D = 45$ on the centerline, normalized by the fuel mass fraction in the jet. Though there is some sensitivity to the reaction progress with the coflow temperature, no temperature in the studied range can adequately predict the reaction progress. Also, there is little difference between both of these chemical mechanisms throughout this coflow temperature range.

In conclusion, these sensitivity studies reveal that none of the investigated parameters yields accurate calculations of the observed reaction progress in PM1-200; therefore, diagnostic calculations are next performed to determine if the reaction rates are in fact overpredicted.

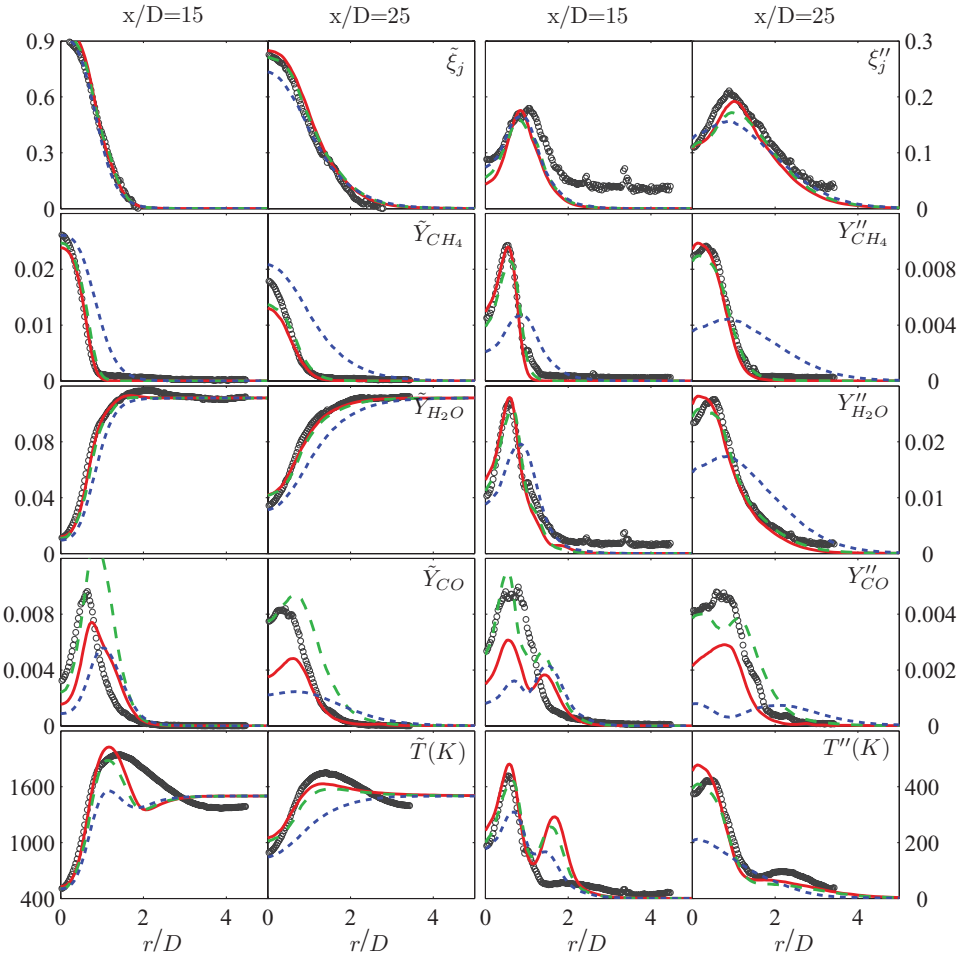

Figure 5. Radial profiles of Favre mean and rms mass fractions (Y) and temperature (T) in PM1-50 at $x/D = 15$ and $x/D = 25$. Open circles are measurements, lines are calculations for different values of f_R: solid (red), $f_R = 1$, unperturbed; dashed (green), $f_R = 0.2$, attenuated; dotted (blue), $f_R = 0$, inert.

4.3. *Diagnostic tests on the chemical reaction timescale*

Additional diagnostic calculations of PM1-50 and PM1-200 are performed in which all chemical reaction rates are attenuated by a constant factor f_R. Thus, $f_R = 1$ corresponds to no modification; $f_R = 0$ corresponds to inert mixing; and the values $f_R = 0.1$, 0.2, and 0.5 are also investigated. It is not suggested that the reaction mechanism has an uncertainty of 10 (as implied by $f_R = 0.1$). Instead, these calculations are performed as a way to shed light on the observed discrepancies.

Scalar fields for PM1-50 are shown in Figure 5 for three values of f_R at $x/D = 15$ and $x/D = 25$. There are three principal observations from this figure. First, the base $f_R = 1$ displays good agreement for mean and rms jet mixture fraction, and good agreement for major species and temperature with the exception of the small region near the centerline. Second, slowing down the chemistry by a factor of 5 ($f_R = 0.2$) has minor consequences

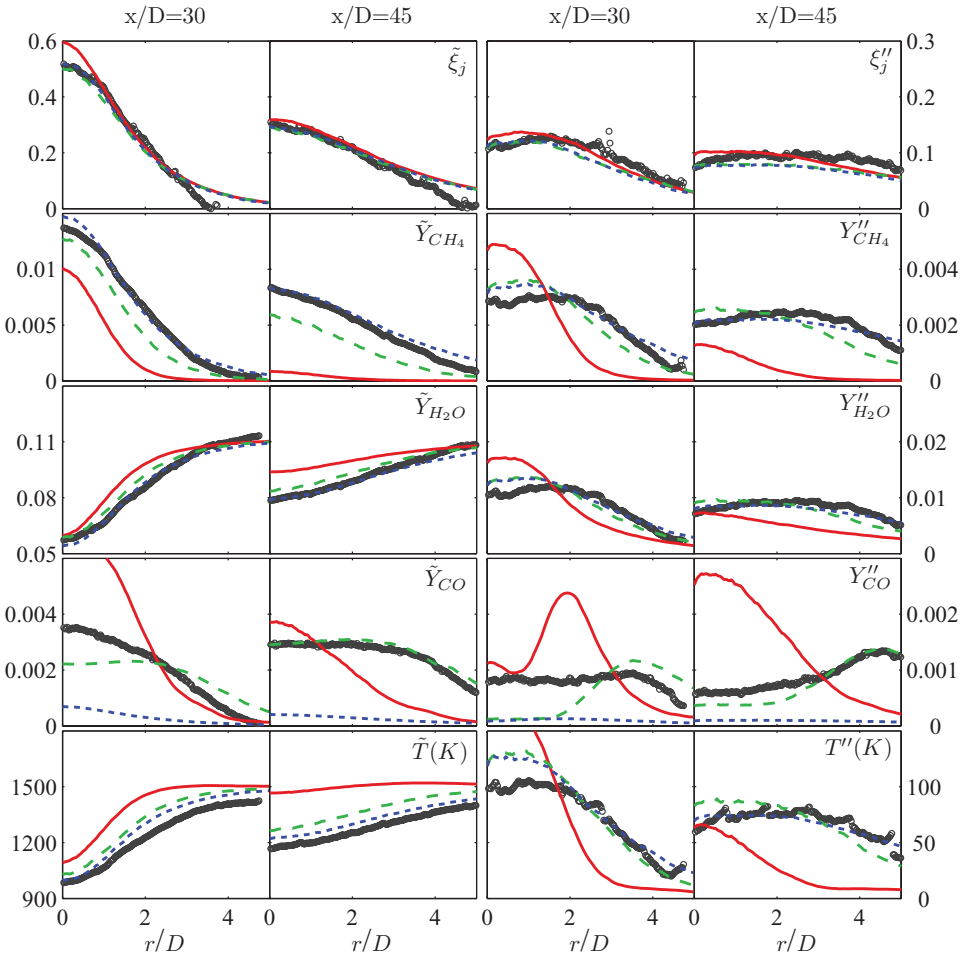

Figure 6. Radial profiles of Favre mean and rms mass fractions (Y) and temperature (T) in PM1-200 at $x/D = 30$ and $x/D = 45$. Open circles are measurements, lines are calculations for different values of f_R: solid (red), $f_R = 1$, unperturbed; dashed (green), $f_R = 0.2$, attenuated; dotted (blue), $f_R = 0$, inert.

in this flame; the major species are not much changed, and only the minor species such as CO show significant sensitivity to f_R. Third, the inert case ($f_R = 0$) clearly overpredicts the amount of fuel and underpredicts the amount of products and the temperature downstream, and therefore this provides evidence that reaction levels are significant in PM1-50. Comparison to the inert case also demonstrates the effect of the heat release from reaction to the temperature field. In the unperturbed case, the temperature field can be around 500 K greater than that of the inert case, suggesting that there is sizable impact of the reaction to the temperature field.

Results for PM1-200 using the same three values of f_R are presented at $x/D = 30$ and $x/D = 45$ in Figure 6. The base case demonstrates good predictions of mean and rms mixture fractions, but drastically underpredicts fuel and overpredicts products and temperature. Unlike PM1-50, PM1-200 is sensitive to the value of f_R; there are significant differences when the reaction rates are slowed by a factor of 5 ($f_R = 0.2$). In this case,

the fuel levels are still slightly underpredicted, but are improved from the base case. Similarly, the product levels and temperature show improvement. The CO levels in the slowed chemistry case show good agreement at this location. The inert case yields the best predictions of mean and rms for major species and temperature at this location. Inevitably, in the inert case, the CO levels are not predicted. A very important conclusion from this diagnostic test is that the inert case provides strong evidence that the amount of reaction occurring in PM1-200 is small, compared to both that in PM1-50 and that in the base case calculations of PM1-200.

4.4. *Analysis of finite-rate chemistry effects*

4.4.1. *Laminar flame calculations*

The nature of the combustion in these flames is examined through the behavior of the minor species CO and OH as functions of temperature. First, simpler laminar flames are analyzed at conditions similar to those in the PPJB. Two primary laminar flames are considered: an opposed flow flame of the jet and the pilot compositions and an opposed flow flame of the jet and the coflow compositions. All of the following calculations are performed using the commercial software CHEMKIN 4.1 with the 53-species GRI3.0 [30] chemical mechanism. In the results presented, the mixture-averaged formulation is used for the evaluation of transport properties and thermal diffusion is accounted for. The evaluation of transport properties by the mixture-averaged formulation has been compared to that by the full multicomponent formulation, and the difference has been found to be negligible at this level of comparison.

In regions where the jet is heavily shielded by the pilot (i.e., near the inlet plane), the influence of the coflow stream is small and the combustion is dominated by the pilot and the jet. This region is analyzed by considering the opposed flow of two streams, denoted A and B, with velocities v_A and v_B, separated by a distance d. The composition of stream A is taken to be the jet composition, and the composition of stream B is taken to be the pilot composition. The stream compositions are those of the pilot and jet, as indicated by Table 1.

The imposed strain rate, a, is defined by $a = (v_A + v_B)/(d \times g)$, where g is a factor determining relative timescales of the chemistry and the flow. A large number of calculations spanning a broad range of values of a is presented in Figure 7, showing the primary quantity of interest, the CO mole fraction, X_{CO} versus temperature. In the cases of extremely high strain rate, the chemical timescale is much slower than the flow timescale, and thus no reaction takes place. The values of X_{CO} in this case lie on the mixing line between streams A and B. On the other extreme of very low strain rate, the jet mixture reacts with little or no mixing, and mixing then proceeds between the two reacted compositions. The behavior in between these extremes is non-trivial, and there exists a strain rate at which the peak X_{CO} is maximized over all strain rates. The reaction moves to higher T as a increases.

In regions where the presence of the pilot is insignificant (i.e., far downstream of the inlet plane), the combustion is dominated by the coflow and the jet. This case is examined by considering the opposed flow of two streams, A and B, where the composition of stream A is taken to be the jet composition, and the composition of stream B is taken to be the coflow composition. The stream compositions are those of the jet and the coflow from Table 1.

The values of X_{CO} versus temperature of the jet-coflow flames are shown in Figure 8 for a large range of imposed strain rates. In this case, the limit of high strain rates bring

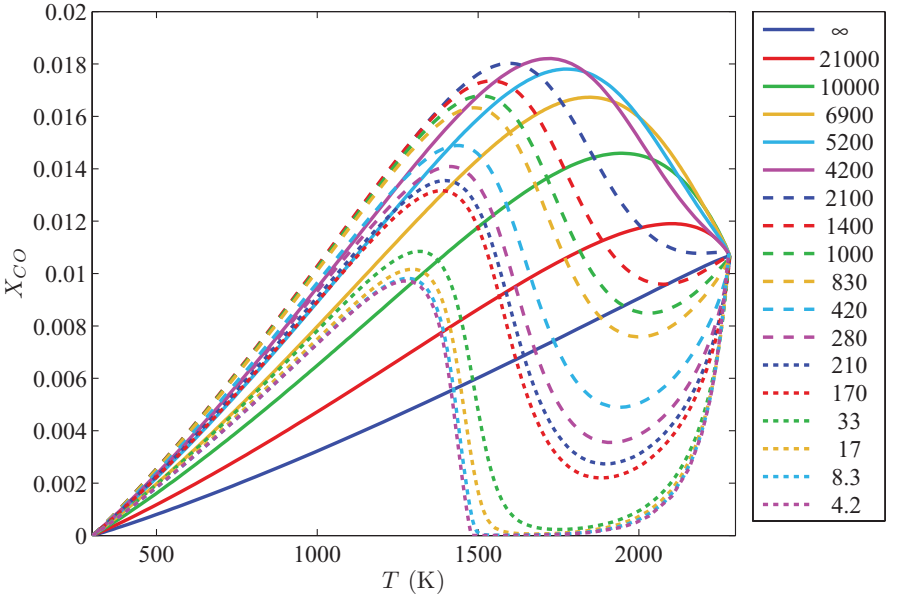

Figure 7. Mole fraction of CO versus temperature for laminar opposed flow flames of the jet and pilot compositions. The imposed strain rate, a, for each calculation is indicated in the legend in units of s^{-1}.

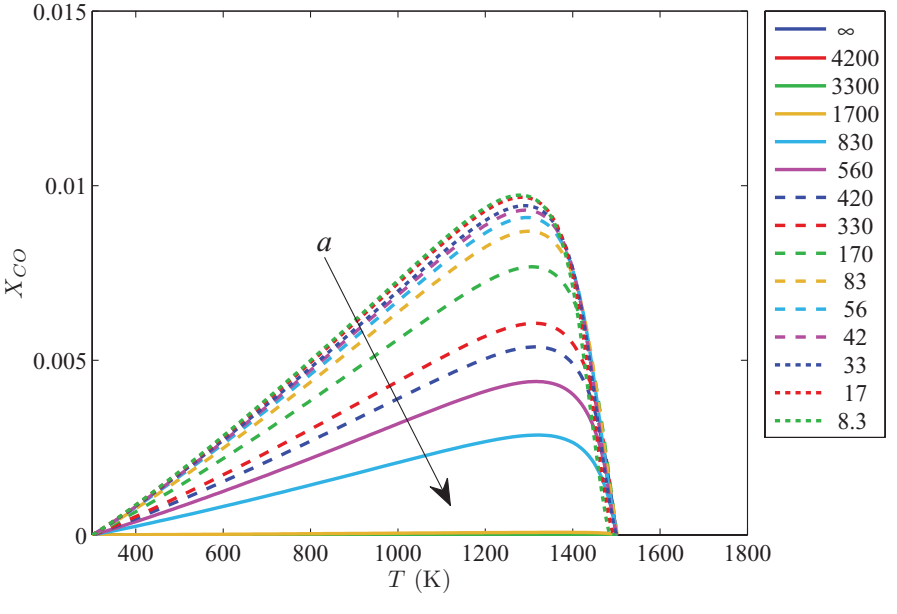

Figure 8. Mole fraction of CO versus temperature for laminar opposed flow flames of the jet and coflow compositions. The imposed strain rate, a, for each calculation is indicated in the legend in units of s^{-1}, and the arrow indicates the direction of increasing a.

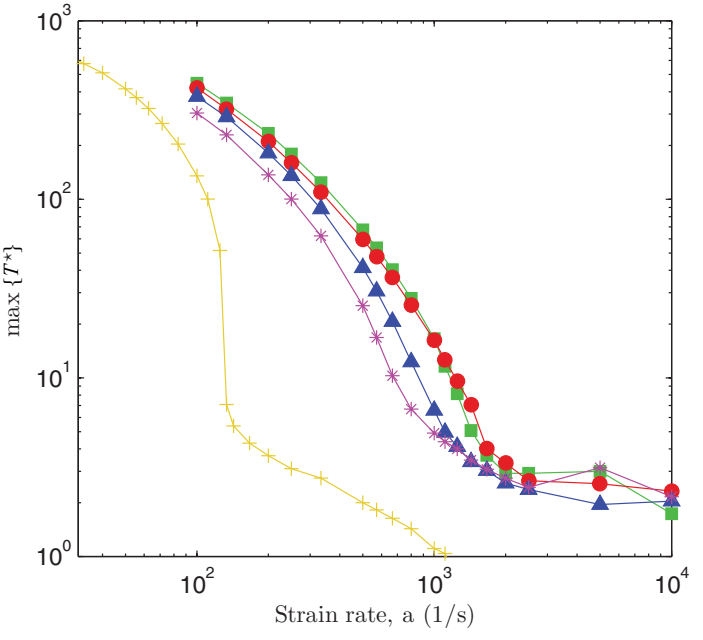

Figure 9. The quantity $\max\{T^\star\}$ as a function of imposed strain rate in laminar jet-coflow flames for different chemical mechanisms. The quantity $T^\star(x)$ is defined as $T^\star(x) = T(x) - T_{\text{mix}}(x)$ where $T_{\text{mix}}(x)$ is the temperature in the case of inert mixing between the streams. The chemical mechanisms are represented by the following symbols: squares are USC-mech-II; circles are GRI3.0; triangles are DRM-22; asterisks are UCSD; plus signs are Correa.

the X_{CO} to zero since there is no CO present initially in either stream. Unlike the pilot-jet laminar flames, the peak X_{CO} occurs near the limit of very low strain rate in the jet-coflow flames.

In the PDF calculations, the overprediction of reaction progress is primarily confined to the jet-coflow region. For this reason, the laminar jet-coflow flames are studied in greater detail. The extinction behavior for these flames is shown in Figure 9 through the quantity $\max\{T^\star\}$, where $T^\star(x) = T(x) - T_{\text{mix}}(x)$ and $T_{\text{mix}}(x)$ is the temperature in the case of inert mixing between the streams. Several chemical mechanisms are evaluated, including USC-mech-II [32], GRI3.0 [30], DRM-22 [33], the UCSD mechanism [31], and a skeletal C_1 mechanism used by Correa [34,35]. For all mechanisms, except possibly for that of Correa, there is no sharp extinction.

This extinction behavior is consistent with that mentioned in [36]. For a flame of premixed reactants against hot products, there is a critical temperature of the hot products above which there is no sharp extinction. Instead of the usual S-shaped curve with a definite extinction strain rate, the curve is monotonic and there is no definite extinction strain rate.

It is noted that the only mechanism that is appreciably slower in the laminar flame calculations is that of Correa. In the PDF sensitivity studies (Figures SM-54–59), this mechanism yields slightly less fuel consumption; however, even for this mechanism the reaction progress is largely overpredicted. Thus, the laminar jet-coflow flames do show a variation with chemical mechanism that is consistent with what is observed in the PDF calculation sensitivity studies. However, in order for the chemical mechanism to be the sole

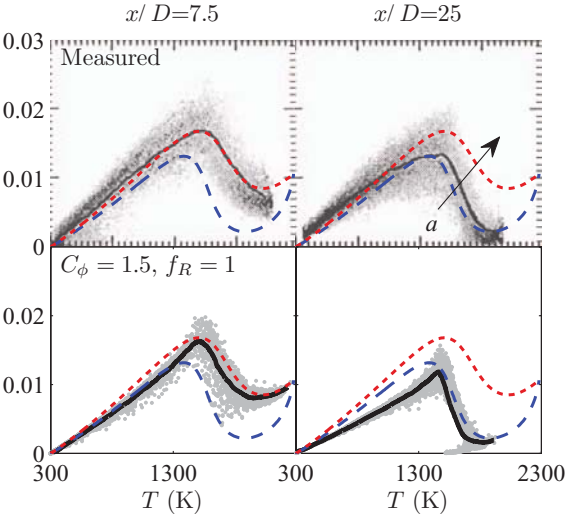

Figure 10. Mole fraction of CO versus temperature in PM1-50. Left plots, $x/D = 7.5$; right plots, $x/D = 25$; top plots, experiments; bottom plots, PDF calculations (base case). Solid line is the conditional mean, and other lines are laminar jet-pilot flames of imposed strain rate: dashed (blue), $a = 160$ s^{-1}; dotted (red), $a = 1000$ s^{-1}. The arrow indicates the direction of increasing a.

cause of the discrepancy in reaction progress, the behavior of the corresponding jet-coflow flames would most likely be radically different, with extinction strain rates even less than that of the Correa mechanism.

4.4.2. *Predictions of CO and OH in turbulent flames*

A comparison is now made between the laminar flame calculations and the PDF calculations in terms of the radicals CO and OH. Shown in Figure 10 are scatter plots of CO mole fraction, X_{CO}, versus temperature at two axial locations for PM1-50. The particles shown in these figures are those whose radial location is between the centerline and the half-width based on the mean jet mixture fraction. In the calculations at $x/D = 7.5$, the ensemble mean coflow mixture fraction, $\langle \xi_c \rangle$, is very small, indicating that fluid originates primarily from the jet and pilot. As in [12], it is observed that X_{CO} conditioned on temperature, $\langle X_{\mathrm{CO}}|T \rangle$, resembles that in a laminar opposed flow flame of the jet and the pilot compositions. Such a calculation with an imposed strain rate, a, of 1000 s^{-1} is found to match both measured and calculated $\langle X_{\mathrm{CO}}|T \rangle$ at $x/D = 7.5$.

The CO versus T behavior for both the calculations and the experiments of PM1-50 shares some common features with that in the stratified flames, particularly the flame fnh6, studied in [37]. Here, in PM1-50, the lean (equivalence ratio of 0.5) methane–air jet interacts with the stoichiometric methane–air pilot. The flame fnh6 consists of a stratification of methane–air ranging in equivalence ratio from 0.37 to 1.10. In the CO versus T behavior in both flames, there is an intermediate temperature range at which the CO mole fractions peak. In fnh6, however, the peak CO mole fractions observed are generally larger, possibly a result of the richer equivalence ratio conditions.

At $x/D = 25$ in PM1-50, $\langle \xi_c \rangle$ is still small at 0.1, and a laminar opposed flow flame of the jet and pilot at $a = 160$ s^{-1} corresponds well with the observed $\langle X_{\mathrm{CO}}|T \rangle$. The

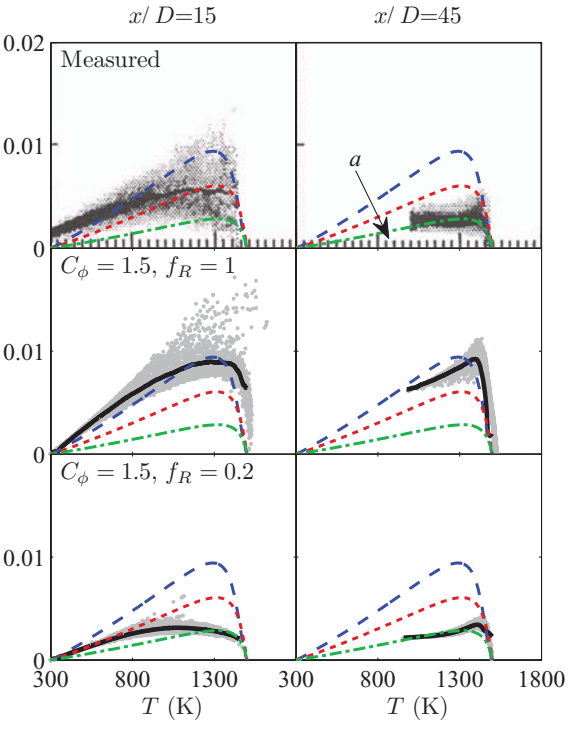

Figure 11. Mole fraction of CO versus temperature in PM1-200. Left plots, $x/D = 15$; right plots, $x/D = 45$; top row, experiments; bottom rows, PDF calculations (middle row, base case; bottom row, attenuated); Solid line is the conditional mean, and other lines are laminar jet-coflow flames of imposed strain rate: dashed (blue), $a = 30\ s^{-1}$; dotted (red), $a = 330\ \mathrm{s}^{-1}$; dashed-dotted (green), $a = 830\ \mathrm{s}^{-1}$. The arrow indicates the direction of increasing a.

decreasing strain rate in the laminar calculations is consistent with the idea that the scalar dissipation rate of a conserved passive scalar is generally decreasing downstream in this flame, considering the approximate proportionality between strain rate and scalar dissipation rate. The agreement between the measurements, PDF calculations, and laminar calculations suggests that the scalar dissipation rate implied by the mixing model may be reasonable in the base case calculations of PM1-50.

Scatter plots of X_{CO} versus temperature for PM1-200 are shown in Figure 11. In PM1-200, the ensemble mean pilot mixture fraction is small (0.07 at $x/D = 15$ and yet smaller at $x/D = 45$). This shows that the fluid is dominantly from the jet and coflow, and hence, comparisons are made with laminar opposed flow flames of these two streams. Note that here (PM1-200, Figure 11), the two relevant streams are the jet and the coflow; whereas for PM1-50 (Figure 10), they are the jet and the pilot.

In general, the $\langle X_{\mathrm{CO}}|T\rangle$ in PM1-200 (Figure 4) is lower than that in PM1-50 (Figure 3) as a result of both the extent of the pilot stream influence and the difference in the scalar dissipation rates between the two flames. Unlike PM1-50, PM1-200 contains few particles above a temperature of 1500 K, providing further evidence of small pilot presence at these locations.

The measured $\langle X_{\mathrm{CO}}|T\rangle$ resembles that in a laminar flame at $a = 330\ \mathrm{s}^{-1}$ at $x/D = 15$, and $a = 830\ \mathrm{s}^{-1}$ at $x/D = 45$. The base case PDF calculations overpredict $\langle X_{\mathrm{CO}}|T\rangle$ by

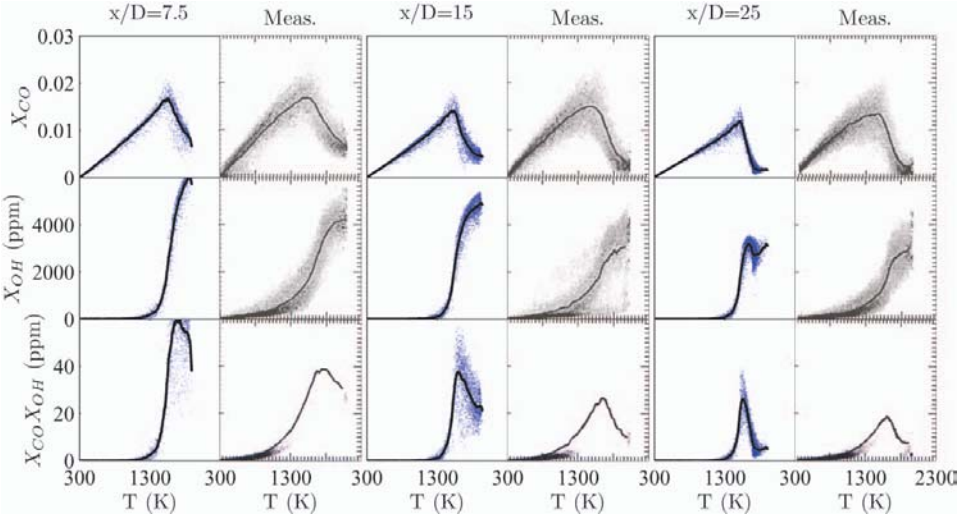

Figure 12. Scatter plots of CO mole fraction (top), OH mole fraction (middle), and the product of CO and OH mole fractions (bottom) in flame PM1-50 versus temperature. Axial locations are $x/D = 7.5$ (left two plots), $x/D = 15$ (middle two plots), and $x/D = 25$ (right two plots). For each axial location, the left-hand plots are calculations and the right-hand plots are measurements. The solid line indicates the conditional mean.

a factor of 2 compared to the measurements. The values of $\langle X_{\mathrm{CO}}|T\rangle$ in the base case are similar to those in a laminar flame of much lower strain rate, about 30 s^{-1}, which may suggest that the scalar dissipation rate implied by the mixing model is underpredicted in the base case.

Figure 11 also shows the calculations with f_R of 0.2. In these calculations, $\langle X_{\mathrm{CO}}|T\rangle$ appears well predicted, particularly at $x/D = 45$. This artificial modification to the chemical reaction timescale alters $\langle X_{\mathrm{CO}}|T\rangle$ in a way different than any value of C_ϕ or mixing model does (Figures SM-36–53). The values of $\langle X_{\mathrm{CO}}|T\rangle$ measured and computed with $f_R = 0.2$ are consistent with a laminar calculation of strain rate about 10 times greater than that in the laminar calculation consistent with the base case. Because the scalar dissipation rate is primarily controlled by the mixing model, these observations suggest that it is the mixing models which perform inadequately at the conditions of PM1-200.

The product of CO and OH mole fractions, $X_{\mathrm{CO}}X_{\mathrm{OH}}$, serves as an indicator of a general product formation rate as in [11, 12], assuming that most of the CO_2 is formed from the reaction CO+OH $\rightarrow$ CO_2+H. In Figure 12, scatter plots of X_{CO}, X_{OH}, and $X_{\mathrm{CO}}X_{\mathrm{OH}}$ are shown from the base case calculations of PM1-50 and compared to the measurements. It is observed as before that the X_{CO} is generally well-predicted as a function of temperature for this flame, and the trend in peak $\langle X_{\mathrm{CO}}|T\rangle$ decreasing downstream is represented well in the calculations. The calculations of X_{OH} are slightly overpredicted compared to the measurements; however, the trend in $\langle X_{\mathrm{OH}}|T\rangle$ decreasing downstream is still captured in the calculations. There is a large sensitivity of X_{OH} to temperature at $T = 1400$ K, and consequently, when the product $X_{\mathrm{OH}}X_{\mathrm{CO}}$ is formed, there is a significant overprediction at $T = 1400$ K.

The mole fraction product $X_{\mathrm{CO}}X_{\mathrm{OH}}$ conditioned on a temperature of 1400 K is shown in Figure 13 as a function of axial distance for both flames. This quantity is considered to be

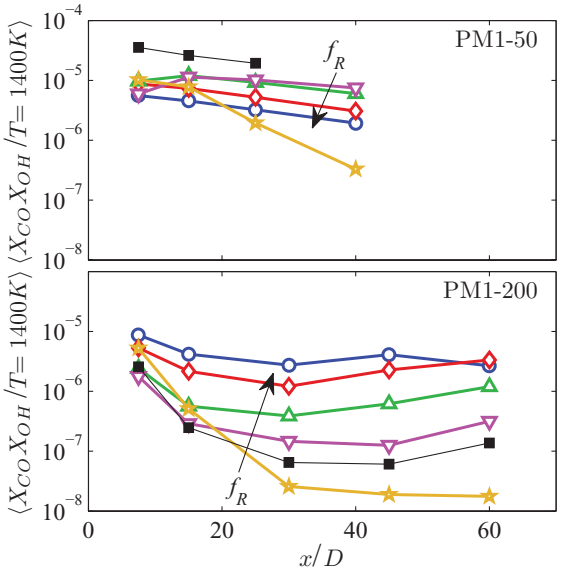

Figure 13. Product of CO and OH mole fraction conditioned on a temperature of 1400 K for the two flames presented from this flame series. Filled squares are measurements, PDF calculations of different values of f_R are open symbols: circles (blue), $f_R = 1$, unperturbed; diamonds (red), $f_R = 0.5$; triangles (green), $f_R = 0.2$; upside-down triangles (magenta), $f_R = 0.1$; stars (yellow), $f_R = 0$, inert. The arrows indicate the direction of increasing f_R.

a comprehensive representation for this flame series in that the trend downstream reflects the observed changes in luminosity.

The trend in PM1-50 is represented well with $f_R = 1$, although the magnitude is largely underpredicted as explained previously. In PM1-200, however, $X_{\mathrm{CO}}X_{\mathrm{OH}}$ is overpredicted by two orders of magnitude in the base case. It is important to consider that none of the sensitivity studies with $f_R = 1$ yield even the correct order of magnitude of this quantity. The large sensitivity in PM1-200 to f_R is shown in Figure 13, and $X_{\mathrm{CO}}X_{\mathrm{OH}}$ is predicted reasonably only when the chemistry is slowed by a factor of 5 or 10. Additionally, the slowed cases provide the correct order of magnitude and axial location for the small region of increased product formation observed near x/D of 60.

4.4.3. *Quantification of reaction progress*

In order to quantify and to compare the level of reaction progress in these flames, a reaction index is introduced. The reaction index based on temperature, R_T, is defined for each particle, i, according to $R_T^i = (T^i - T_{\mathrm{mix}}^i)/(T_{\mathrm{eq}}^i - T_{\mathrm{mix}}^i)$ where T^i is the temperature of particle i, T_{mix}^i is the temperature of an inert mixture at the mixture fractions of particle i, and T_{eq}^i is the equilibrium temperature of particle i. A reaction index of zero corresponds to an unburnt particle, and a reaction index of unity corresponds to a particle at equilibrium. It should be noted that this quantity is poorly defined when $T_{\mathrm{eq}}^i = T_{\mathrm{mix}}^i$, which occurs for streams initially at equilibrium, for example, both the pilot and the coflow here. So when this quantity is examined, only particles with sufficiently large jet mixture fractions are considered.

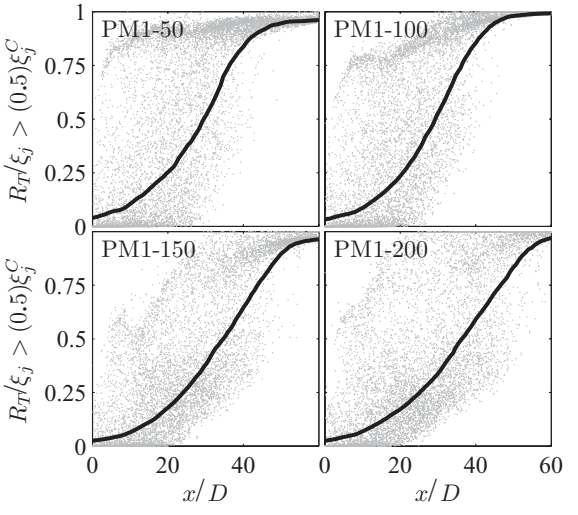

Figure 14. Reaction index based on temperature, R_T, for particles in base case calculations of all flames in this series. The mass-weighted mean conditioned on axial location is indicated by the solid line, and the particle values are indicated by the light dots. Particles are conditioned on a jet mixture fraction greater than half the mean jet mixture fraction on the centerline.

The particle values of R_T are shown for the base case of all flames in this series in Figure 14. The particles are conditioned on a jet mixture fraction, ξ_j, greater than half the mean jet mixture fraction on the centerline, ξ_j^C. This conditioning has been compared to conditioning on particles originating from the jet, and the results are similar at this level of comparison. Figure 14 shows that for all four flame calculations, there is little difference in

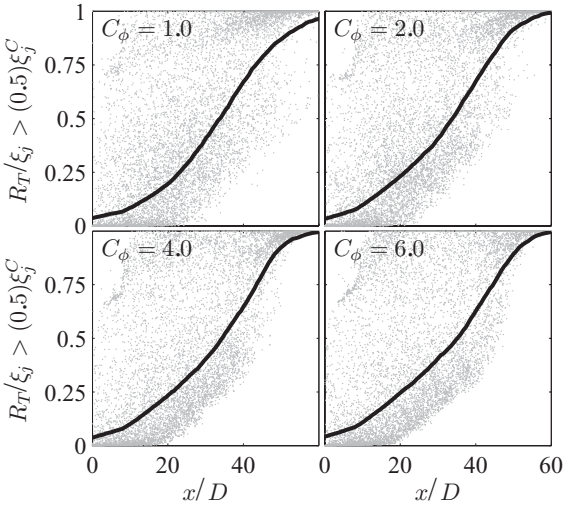

Figure 15. Reaction index based on temperature, R_T, for particles in calculations of PM1-200 for varying levels of C_ϕ, indicated in the top left corner of each plot. The mass-weighted mean conditioned on axial location is indicated by the solid line, and the particle values are indicated by the light dots. Particles are conditioned on a jet mixture fraction greater than half the mean jet mixture fraction on the centerline.

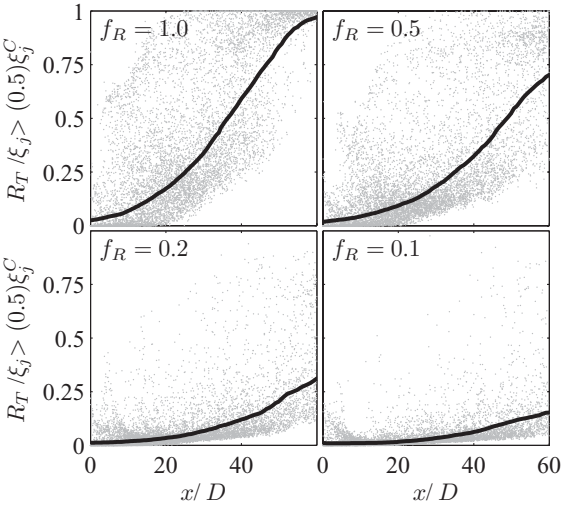

Figure 16. Reaction index based on temperature, R_T, for particles in diagnostic test calculations of PM1-200 for varying reaction rate attenuation factors, f_R, indicated in the top left corner of each plot. The mass-weighted mean conditioned on axial location is indicated by the solid line, and the particle values are indicated by the light dots. Particles are conditioned on a jet mixture fraction greater than half the mean jet mixture fraction on the centerline.

the evolution of reaction progress downstream, which is most likely incorrect based on the experimental observations.

Figure 15 shows the same information for different values of the mixing model constant, C_ϕ, in calculations of PM1-200. As summarized in the sensitivity studies, there is little sensitivity to the mixing model constant. Since the reaction progress is generally determined by the scalar dissipation rate, it can be inferred that the scalar dissipation rate is largely uninfluenced by the mixing models and constants; this behavior is unlike several previous calculations of non-premixed flames [5], in which the mixing models and constants significantly influence the scalar dissipation rate.

Lastly, Figure 16 shows R_T from the diagnostic tests of PM1-200 in which the reaction rates are attenuated. From these tests, a more likely level of reaction index can be determined for this flame. Based on the previous comparisons, PM1-200 is better calculated with f_R of 0.1 or 0.2. Therefore it might be assumed that the reaction index for this flame is more realistically near the levels of that determined for f_R of 0.1 or 0.2, which is generally lower by a factor of about 5 from the base case calculations.

5. Conclusions

Calculations of a challenging series of lean piloted premixed jet flames have been performed using the PDF method. The following conclusions can be drawn from this study:

1. With the base case models and constants, the PDF method provides accurate calculations of PM1-50 with the exception of an overprediction in reaction progress localized in a small region near the centerline.
2. For PM1-200, with its increased jet velocity, the base case computations overpredict the extent of reaction much more severely than in PM1-50.

3. An extensive set of sensitivity studies on PM1-200 demonstrates that no set of models or parameters is able to predict the correct extent of reaction. PM1-200 is shown to be much more sensitive to the chemical reaction attenuation factor than is PM1-50. More accurate calculations of PM1-200 are obtained only by artificially slowing the chemistry.
4. Thorough studies are performed to show that transport is calculated accurately, and additional sensitivity studies show that the chemistry is insensitive to a wide variety of chemical mechanisms. By process of elimination, the mixing models are identified as a likely cause for the modeling deficiencies evident at these conditions.
5. The finite-rate chemistry effects are shown to be significant in this flame series. The PDF method is reaffirmed as a useful tool for investigating these effects and is shown to be computationally feasible for performing extensive sensitivity studies.

As in previous PDF calculations of premixed flames [10, 38], an aspect of the mixing model called into question is the specification of the mechanical-to-scalar timescale ratio, C_ϕ. These previous works have reported increased success with values of C_ϕ nearly an order of magnitude larger than the typically used values (i.e., C_ϕ in the range of 6–12, compared to typical values of C_ϕ in the range of 1.5–2.5). In the sensitivity studies of PM1-200, it is learned that increasing C_ϕ does in fact decrease the overprediction in reaction progress (Figure SM-36-41). However, even a value of C_ϕ as large as 12 is unable to match the observed reaction progress. Furthermore, increasing C_ϕ degrades the calculation of the mixture fraction fields, and the mixture fraction fields are computed most accurately with C_ϕ in the range of 1.5–2.0. The aforementioned previous works have also indicated increased success when the mechanical-to-scalar timescale ratio is specified based on a model for the scalar dissipation rate. This type of procedure has not yet been investigated in the PPJB flame series. However, it should be noted that the PPJB flames are quite different from the aforementioned premixed flames; for instance, the Damköhler numbers are significantly smaller in the PPJB flames, and it is concluded in [10] that the influence of the chemical reaction on the scalar dissipation rate is most considerable in the high Damköhler number limit.

The increase in jet velocity from 50 m/s in PM1-50 to 200 m/s in PM1-200 has several effects: the flow timescales (and hence the Damköhler numbers) are reduced (by about a factor of 4); the pilot provides less shielding in that it is fully entrained in a significantly shorter distance; and (perhaps of least significance) the Reynolds number is increased by a factor of 4. It is conjectured that the reduced shielding is the dominant effect. This could be tested experimentally by increasing the pilot velocity to maintain the same ratio to the jet velocity (as done in the Barlow–Frank flames [39]). Indeed a PDF calculation of PM1-50 with $f_R = 0.25$ corresponds very closely to a calculation of PM1-200 with the pilot velocity increased by a factor of 4; and it is evident that PM1-50 with $f_R = 0.2$ (Figure 5) is very different from PM1-200 (Figure 6).

Acknowledgements

This work was supported in part by Air Force Office of Scientific Research, Grant FA9550-09-1-0047. This research was made with Government support under and awarded by DoD, Air Force Office of Scientific Research, National Defense Science and Engineering Graduate (NDSEG) Fellowship, 32 CFR 168a.

References

[1] S.B. Pope, *PDF methods for turbulent reactive flows*, Prog. Energy Combust. Sci. 11 (1985), pp. 119–192.

[2] J.Y. Chen, W. Kollmann, and R.W. Dibble, *PDF modeling of turbulent nonpremixed methane jet flames*, Combust. Sci. Technol. 64 (1989), pp. 315–346.
[3] V. Saxena and S.B. Pope, *PDF simulations of turbulent combustion incorporating detailed chemistry*, Combust. Flame 117 (1999), pp. 340–350.
[4] R.P. Lindstedt, S.A. Louloudi, and E.M. Váos, *Joint scalar probability density function modeling of pollutant formation in piloted turbulent jet diffusion flames with comprehensive chemistry*, Proc. Combust. Inst. 28 (2000), pp. 149–156.
[5] J. Xu and S.B. Pope, *PDF calculations of turbulent nonpremixed flames with local extinction*, Combust. Flame 123 (2000), pp. 281–307.
[6] R.P. Lindstedt and S.A. Louloudi, *Joint scalar transported probability density function modeling of turbulent methanol jet diffusion flames*, Proc. Combust. Inst. 29 (2002), pp. 2147–2154.
[7] R.R. Cao, S.B. Pope, and A.R. Masri, *Turbulent lifted flames in a vitiated coflow investigated using joint PDF calculations*, Combust. Flame 142 (2005), pp. 438–453.
[8] R.R. Cao, H. Wang, and S.B. Pope, *The effect of mixing models in PDF calculations of piloted jet flames*, Proc. Combust. Inst. 31 (2007), pp. 1543–1550.
[9] T. Hůlek and R.P. Lindstedt, *Computations of steady-state and transient premixed turbulent flames using pdf methods*, Combust. Flame 104 (1996), pp. 481–504.
[10] R.P. Lindstedt and E.M. Váos, *Transported PDF modeling of high-Reynolds-number premixed turbulent flames*, Combust. Flame 145 (2006), pp. 495–511.
[11] M.J. Dunn, A.R. Masri, and R.W. Bilger, *A new piloted premixed jet burner to study strong finite-rate chemistry effects*, Combust. Flame 151 (2007), pp. 46–60.
[12] M.J. Dunn, A.R. Masri, R.W. Bilger, R.S. Barlow, and G.H. Wang, *The compositional structure of highly turbulent piloted premixed flames issuing into a hot coflow*, Proc. Combust. Inst. 32 (2009), pp. 1779–1786.
[13] M.J. Dunn, A.R. Masri, R.W. Bilger, and R.S. Barlow, *Finite rate chemistry effects in highly sheared turbulent premixed flames*, Flow Turbul. Combust. 1386-6184 (2010), pp. 1–28.
[14] G.A. Richards, M.M. McMillian, R.S. Gemmen, W.A. Rogers, and S. R. Cully, *Issues for low-emission, fuel-flexible power systems*, Prog. Energy Combust. Sci. 27 (2001), pp. 141–169.
[15] S.B. Pope, *Turbulent Flows*, Cambridge University Press, Cambridge, 2000.
[16] D.C. Haworth and S.B. Pope, *A generalized Langevin model for turbulent flows*, Phys. Fluids 29 (1986), pp. 387–405.
[17] P.R. Van Slooten, Jayesh, and S.B. Pope, *Advances in PDF modeling for inhomogeneous turbulent flows*, Phys. Fluids 10 (1998), pp. 246–265.
[18] S. Subramaniam and S.B. Pope, *A mixing model for turbulent reactive flows based on Euclidean minimum spanning trees*, Combust. Flame 115 (1998), pp. 487–514.
[19] S.B. Pope, *Computationally efficient implementation of combustion chemistry using in situ adaptive tabulation*, Combust. Theory Model. 1 (1997), pp. 41–63.
[20] L. Lu and S.B. Pope, *An improved algorithm for in situ adaptive tabulation*, J. Comp. Phys. 228 (2009), pp. 361–386.
[21] P. Jenny, M. Muradoglu, K. Liu, S.B. Pope, and D.A. Caughey, *PDF simulations of a bluff-body stabilized flow*, J. Comp. Phys. 169 (2001), pp. 1–23.
[22] M. Muradoglu, S.B. Pope, and D.A. Caughey, *The hybrid method for the PDF equations of turbulent reactive flows: consistency conditions and correction algorithms*, J. Comp. Phys. 172 (2001), pp. 841–878.
[23] M. Muradoglu, K. Liu, and S.B. Pope, *PDF modeling of a bluff-body stabilized turbulent flame*, Combust. Flame 132 (2003), pp. 115–137.
[24] J. Xu and S.B. Pope, *Assessment of numerical accuracy of PDF/Monte Carlo methods for turbulent reactive flows*, J. Comp. Phys. 152 (1999), pp. 192–230.
[25] C.J. Sung, C.K. Law, and J.Y. Chen, *An augmented reduced mechanism for methane oxidation with comprehensive global parametric validation*, Proc. Combust. Inst. 27 (1998), pp. 295–304.
[26] R.L. Curl, *Dispersed phase mixing-theory and effects in simple reactors*, AICHE J. 9 (1963), pp. 175–181.
[27] J. Janicka, W. Kolbe, and W. Kollmann, *Closure of the transport equation for the probability density function of turbulent scalar fields*, J. Non-Equilib. Thermodyn. 4 (1979), pp. 47–66.
[28] J. Villermaux and J.C. Devillon, *Representation de la coalescence et de la redispersion des domaines de segregation dans un fluide par un modele d'interaction phenomenologique*, in *Proc. Second Int. Symp. On Chemical Reaction Engineering*, New York, Elsevier, 1972.

[29] C. Dopazo and E.E. O'Brien, *An approach to the autoignition of a turbulent mixture*, Acta Astronaut. 1 (1974), pp. 1239–1266.
[30] V.V. Lissianski and Z. Qin, available at http://www.me.berkeley.edu/gri-mech.
[31] http://maeweb.ucsd.edu/combustion/cermech.
[32] H. Wang, X. You, A.V. Joshi, S.G. Davis, A. Laskin, F. Egolfopoulos, and C.K. Law, *USC Mech Version II. High-Temperature Combustion Reaction Model of H2/CO/C1-C4 Compounds*, May 2007, available at http://ignis.usc.edu/USC_Mech_II.htm.
[33] A. Kazakov and M. Frenklach, available at http://www.me.berkeley.edu/drm/.
[34] M.D. Smooke and V. Giovangigli, *Reduced kinetic mechanisms and asymptotic approximations for methane–air flames*, Lecture Notes in Physics 384 (1991), pp. 1–47.
[35] S.M. Correa, *A review of NOx formation under gas-turbine combustion conditions*, Comb. Flame 93 (1993), pp. 41–60.
[36] G. Dixon-Lewis, *Structure of laminar flames*, Proc. Combust. Inst. 23 (1990), pp. 305–324.
[37] R.S. Barlow, G.H. Wang, P. Anselmo-Filho, M.S. Sweeney, and S. Hochgrebb, *Application of Raman/Rayleigh/LIF diagnostics in turbulent stratified flames*, Proc. Combust. Inst. 32 (2009), pp. 945–953.
[38] M. Stollinger and S. Heinz, *Evaluation of scalar mixing and time scale models in PDF simulations of a turbulent premixed flame*, Combust. Flame 157 (2010), pp. 1671–1685.
[39] R.S. Barlow and J.H. Frank, *Effects of turbulence on species mass fractions in methane–air jet flames*, Proc. Combust. Inst. 27 (1998), pp. 1087–1095.